Single-entity Electrochemistry Unveils Dynamic Transformation during Tandem Catalysis of Cu_2O and Co_3O_4 for Converting NO_3^- to NH_3

Jian Zhang, Wenhui He, Thomas Quast, João R. C. Junqueira, Sascha Saddeler, Stephan Schulz, and Wolfgang Schuhmann*

Abstract: Electrochemically converting nitrate to ammonia is an essential and sustainable approach to restoring the globally perturbed nitrogen cycle. The rational design of catalysts for the nitrate reduction reaction (NO_3RR) based on a detailed understanding of the reaction mechanism is of high significance. We report a $Cu_2O + Co_3O_4$ tandem catalyst which enhances the NH_3 production rate by ≈ 2.7-fold compared to Co_3O_4 and ≈ 7.5-fold compared with Cu_2O, respectively, however, most importantly, we precisely place single Cu_2O and Co_3O_4 cube-shaped nanoparticles individually and together on carbon nanoelectrodes provide insight into the mechanism of the tandem catalysis. The structural and phase evolution of the individual $Cu_2O + Co_3O_4$ nanocubes during NO_3RR is unveiled using identical location transmission electron microscopy. Combining single-entity electrochemistry with precise nano-placement sheds light on the dynamic transformation of single catalyst particles during tandem catalysis in a direct way.

Introduction

Ammonia (NH_3) is an essential raw material in fertilizers, the chemical industry, and emerging energy conversion processes.[1] Presently, the production of NH_3 relies on the energy-intensive Haber-Bosch process, which is a gas-phase reaction between H_2 and N_2 under high temperature and

pressure.[2] Alternatively, the electrochemical N_2 reduction reaction (NRR) driven by renewable energy is increasingly discussed as a more sustainable route for NH_3 production at room temperature.[3] However, the NRR has suffered an ultra-low yield rate for NH_3 caused by the high dissociation energy of the inherent stable $N\equiv N$ triple bond ($941 \, kJ \, mol^{-1}$),[4] which until now, prevents its practical application.[5] In stark contrast to the NRR, the nitrate (NO_3^-) reduction reaction (NO_3RR) stands out as a promising route due to the relatively lower energy for dissociating $N=O$ double bond ($204 \, kJ \, mol^{-1}$),[6] allowing much faster reaction kinetics for NH_3 production.[7] NO_3^- is widely available in industrial wastewater and groundwater, and hence the NO_3RR can also address environmental pollution problems simultaneously.[8]

Developing a high-performance NO_3RR catalyst based on a rational catalyst design strategy is the prerequisite to achieving highly efficient NO_3^- to NH_3 conversion.[9] "Tandem catalysis" has been successfully reported for complex multi-electron transfer reactions, e.g. the CO_2 reduction reaction, in which the synergistic action of multiple components of a catalyst can break down the sequential reaction steps to optimized active sites catalyzing each step.[10] $*NO_2$ (* denotes a surface-adsorbed species) and the related intermediates are critical for the eight-electrons transfer during the NO_3RR, and hence a tandem strategy can facilitate the NO_3^- to NH_3 conversion.[11] Very recently, we have proposed a Co- and Cu-based tandem catalysts for the NO_3RR, in which the NO_3^- to NH_3 conversion can be divided into an initial NO_3^- reduction step under formation of NO_2^- catalyzed by a Cu phases followed by the NO_2^- to NH_3 conversion performed by the Co phases.[12] However, although our previous report provides experimental evidence for the tandem catalysis of NO_3RR via in situ scanning electrochemical microscopy (SECM), due to the complexity of the multi-metal active phases derived from metal–organic frameworks (MOF) at the nanoscale, the tandem effect of the two catalysts and especially structural re-modelling and interfacial effects due to possible alloying during the reaction need to be further elucidated.[13] More importantly, gaining knowledge about the dynamic evolution of different metal phases during tandem reactions is highly challenging and until now impossible to be directly visualized, which is vital for a deep understanding of tandem catalysis for NO_3RR. In recent years, the development of single entity electrochemistry (SEE)[14] and especially the

[*] J. Zhang, Dr. W. He, Dr. T. Quast, Dr. J. R. C. Junqueira,
Dr. S. Saddeler, Prof. Dr. W. Schuhmann
Analytical Chemistry—Center for Electrochemical Sciences (CES);
Faculty of Chemistry and Biochemistry, Ruhr University Bochum
Universitätsstr. 150, 44780 Bochum (Germany)
E-mail: wolfgang.schuhmann@rub.de

Dr. S. Saddeler, Prof. Dr. S. Schulz
Inorganic Chemistry, Faculty of Chemistry and Center for Nano-integration Duisburg-Essen (Cenide), University of Duisburg-Essen
Universitätsstr. 7, 45141 Essen (Germany)

single-particle-on-the-nanoelectrode technique[15–18] provided direct insight into the intrinsic activity of a given electrocatalyst as well as structural evolution at the nanoscale accessible when combined with identical location TEM.[19] Hence, we consider SEE suitable to unveil the tandem effect between two catalysts during NO_3RR.

In this work, we report $Cu_2O+Co_3O_4$ tandem NO_3RR catalysts obtained by physically mixing of Cu_2O and Co_3O_4 nanocubes. The $Cu_2O+Co_3O_4$ catalyst shows a superior 85.4 % Faradaic efficiency of NH_3 formation (FE_{NH_3}) and a high NH_3 yield rate (Y_{NH_3}) of 12.76 mg h^{-1} cm^{-2} at −0.3 V vs RHE which exceeds that of Co_3O_4 by ≈2.7-fold and that of Cu_2O by ≈7.5-fold, respectively. To provide direct microscopic evidence for tandem catalysis of $Cu_2O+Co_3O_4$ at the nanoscale and the interactions between the Cu_2O and Co_3O_4 nanocubes, we established a carbon nanoelectrode (CNE) platform, which enables us to precisely control the relative locations of single similarly sized Cu_2O and Co_3O_4 nanocubes by means of a micromanipulator arm inside a scanning

electron microscope (SEM). We confirmed the sequential tandem catalysis of single Cu_2O and Co_3O_4 particles on a nanoelectrode and monitored the structural and phase evolution caused by tandem catalysis during the reaction.

Results and Discussion

Performance of Electrochemical Nitrate Conversion

First, the tandem catalyst was prepared by physical mixing of Cu_2O and Co_3O_4 nanocubes on a carbon paper, in the following named $Cu_2O+Co_3O_4$. We deliberately decided to use cubes which are exposing the (1 0 0) lattice to avoid contributions from different lattice orientations and hence different catalytic activity to the overall response. SEM images and energy dispersive X-ray (EDX) mapping (Figure 1a) show randomly distributed Cu_2O and Co_3O_4 nanocubes on the carbon surface. The size of both Cu_2O and
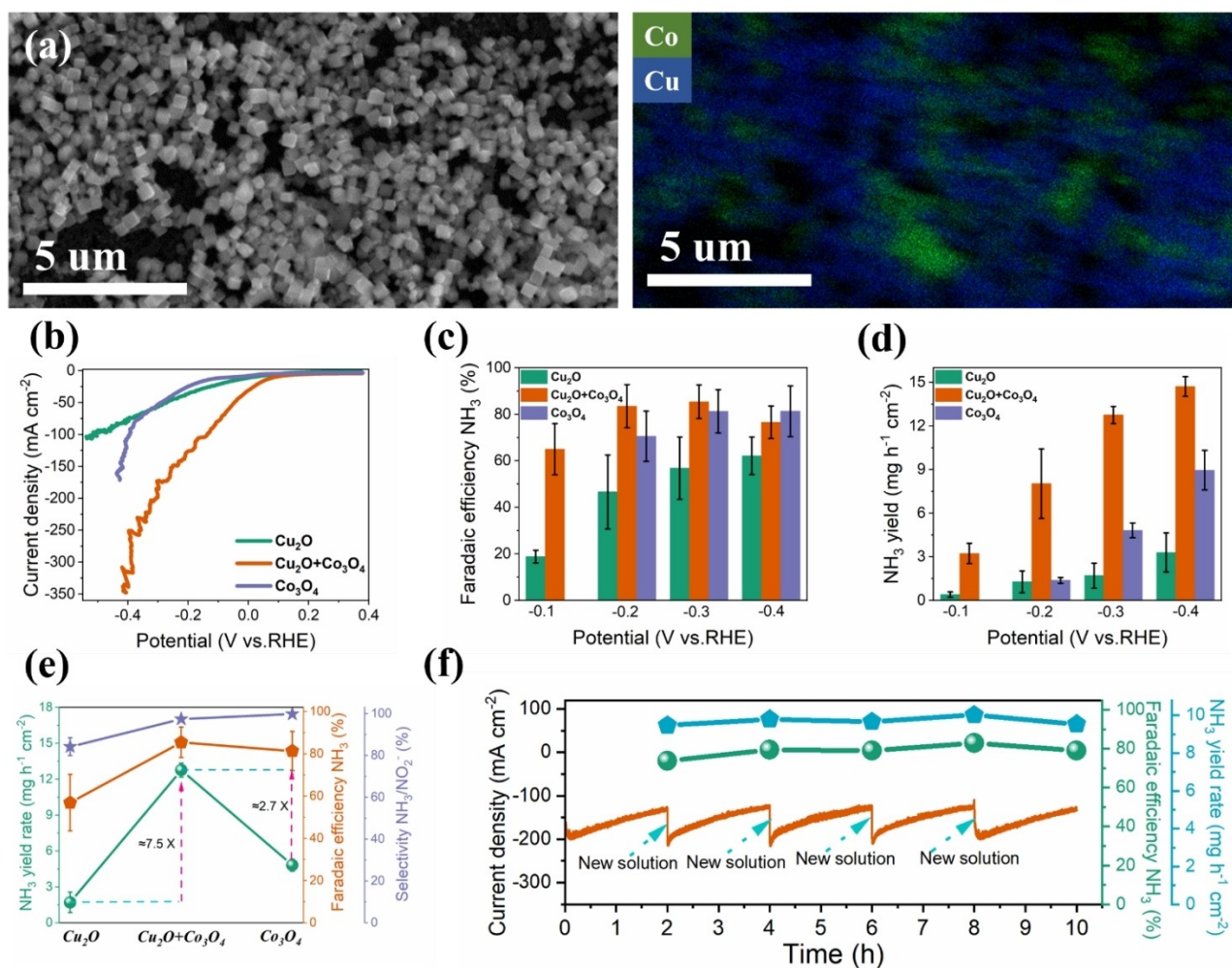

Figure 1. a) SEM image of $Cu_2O+Co_3O_4$ on a carbon paper electrode and corresponding EDX elemental mapping. b) Linear sweep voltammograms (LSV) at a scan rate 5 mV s^{-1} in 0.1 mol L^{-1} NO_3^- and 0.1 mol L^{-1} NaOH. c) Faradaic efficiencies and d) yield rate for NH_3 on Cu_2O, Co_3O_4, and $Cu_2O+Co_3O_4$. Error bars denote the standard deviations from at least three independent measurements. e) Yield rate, FE and selectivity comparisons of Cu_2O, Co_3O_4 and $Cu_2O+Co_3O_4$ at −0.3 V (vs RHE). Error bars denote the standard deviations from at least three independent measurements. f) Chronoamperometric stability test at −0.3 V (vs RHE) and corresponding NH_3 FEs as well as yield rate of $Cu_2O+Co_3O_4$.

Co_3O_4 nanocubes are predominantly in the range of 200–300 nm (Figure S1). EDX confirms the presence of Cu, Co, O and C, with an atomic ratio of Cu to Co of 2.8:1, as determined by inductively coupled plasma mass spectrometry (ICP-MS; Figure S2 and inset of Figure S2). Raman spectra were recorded to gain insight into the phase constitution of the $Cu_2O + Co_3O_4$ electrode showing a series of intense Raman peaks at 216, 415, 485, 523, 525, 621, 629 and 693 cm^{-2}, which can be ascribed to the characteristic vibrational modes of Cu_2O and Co_3O_4 (Figure S3).[20–22]

The NO_3RR catalytic activity was assessed by linear sweep voltammetry (LSV) in 0.1 mol L^{-1} NaOH containing 0.1 mol L^{-1} NO_3^-. The NO_3RR activity of $Cu_2O + Co_3O_4$ electrode can be initially determined by the pronounced increased current density in the presence of NO_3^- compared to bare carbon paper and the less cathodic overpotential as in the absence of NO_3^- (Figure S4). Plots in Figure 1b show that the mixed $Cu_2O + Co_3O_4$ electrode has a much higher current density (normalized by geometric area) than the only Cu_2O or Co_3O_4 modified electrodes, indicating its increased NO_3RR activity. To compare the catalytic activity more precisely, the double-layer capacitance (C_{dl}) as a measure for the electrochemically active surface area (ECSA) was determined and used to normalize the current density (Figure S5). Even after normalization by the C_{dl} (Figure S6), the mixed $Cu_2O + Co_3O_4$ modified electrode exhibited the highest activity. Comparing the required potentials of the electrodes to reach a current density of 20 mA cm^{-2} (kinetic area with negligible impact of mass transfer) normalized by geometric area (Figure S7), we find that the mixed $Cu_2O + Co_3O_4$ catalyst needs an overpotential of 40 mV which is 122 and 209 mV more positive than that of the Cu_2O or the Co_3O_4 modified electrodes, respectively. Furthermore, the overpotentials normalized by the C_{dl} follow a similar trend, indicating that $Cu_2O + Co_3O_4$ exhibits a favourable reaction kinetics towards the NO_3RR.

The Faradaic efficiencies for the products (NH_3 and NO_2^-) of the three electrodes show a significant difference (Figures S8–S11). Cu_2O alone exhibits only 18.8% FE for NH_3, and Co_3O_4 does not produce any NH_3 at −0.1 V. In stark contrast to the single materials, $Cu_2O + Co_3O_4$ shows a relatively higher FE_{NH_3} of 65.1% (Figure 1c), which cannot be explained simply through the individual contributions of Cu_2O and Co_3O_4. Explicitly, Cu_2O exhibits a very high inherent selectivity towards the formation of NO_2^- at −0.1 V. This is also consistent with results of Cu-based NO_3RR catalysts, which desorb *NO_2^- on the Cu surface much easier to form stable NO_2^- thus preventing further reduction to NH_3.[23] $Cu_2O + Co_3O_4$ shows a higher selectivity of 81.2% for NH_3 over NO_2^- at −0.1 V compared to 29.5% selectivity of Cu_2O (Figure S12), suggesting a suppressed NO_2^- but simultaneously boosted NH_3 selectivity on the $Cu_2O + Co_3O_4$ surface. These results perfectly correspond to the characteristics of tandem catalysis, in which NO_2^-, generated from Cu_2O as the primary product, is transferred to the nearby Co_3O_4 surface for subsequent conversion of NO_2^- to NH_3. At more negative applied potentials, the $Cu_2O + Co_3O_4$ exhibits a high NH_3 selectivity suppressing

the NO_2^- selectivity by tandem catalysis hence showing a maximum FE of 85.4% for NH_3 at −0.3 V.

The NH_3 yield rate (Y_{NH_3}) of all three catalysts is presented in Figure 1d. The three electrodes show a linearly increasing Y_{NH_3} with increasing applied negative potentials, and the $Cu_2O + Co_3O_4$ electrode stands out due to the much higher Y_{NH_3} of 3.23, 8.03, 12.76, and 14.72 mg h^{-1} cm^{-2} at −0.1, −0.2, −0.3 and −0.4 V (vs RHE), respectively. The Y_{NH_3}, FE_{NH_3} as well as the selectivity of the three catalysts at a potential of −0.3 V are shown in Figure 1e. The comparison of the Y_{NH_3} shows a volcano shape, and the Y_{NH_3} of $Cu_2O + Co_3O_4$ is ≈2.7-fold that of Co_3O_4 and ≈7.5-fold that of Cu_2O, respectively. The high Y_{NH_3} together with the FE and selectivity toward NH_3 of $Cu_2O + Co_3O_4$ shows its superior performance, which is superior with respect to most recently reported NO_3RR catalysts (Table S1). Furthermore, the durability of $Cu_2O + Co_3O_4$ was investigated by chronoamperometry at a potential of −0.3 V, and the FE_{NH_3}, as well as Y_{NH_3}, were analyzed by collecting the post-electrolysis electrolyte after each 2 h. In Figure 1f, the i-t curve shows a relatively stable trend after replacing with new electrolyte solution each 2 h, and the FE_{NH_3} as well as the Y_{NH_3} in each cycle only fluctuate negligibly indicating high NO_3RR stability.

To determine the origin of the detected NH_3 and to confirm the determined Y_{NH_3}, ^{1}H NMR spectroscopy was applied to investigate the NH_3 formation on $Cu_2O + Co_3O_4$ in more detail (Figure S13).[24] ^{1}H NMR spectra show two typical peaks of $^{15}NH_4^+$ after being electrolyzed in 0.1 mol L^{-1} NaOH containing 0.1 mol L^{-1} $^{15}NO_3^-$, confirming that the formed NH_3 originated from the reduction of NO_3^- (Figure S13c). The amount of $^{14}NH_4^+$ quantified by ^{1}H NMR is close to that determined by UV–Vis spectrophotometry, confirming the reliability of the results (Figure S13d).

A detailed understanding of the intrinsic activity and structure evolution of $Cu_2O + Co_3O_4$ is required to unveil the reaction mechanism which is the basis for the observed superior NO_3RR performance. Deriving the intrinsic activity of a nanosized catalyst material is challenging from the results of macroelectrode experiments due to mass transfer limitations (planar diffusion), local pH changes caused by proton-coupled electron-transfer reactions, and film effects such as the conductivity of the catalyst particle film, the presence of binder materials etc. (Figure 2a).[18,25] Catalyst particles scratched off from a macroelectrode after an electrochemical experiment are not necessarily representative for the evolution of the structural morphology. Hence, to directly establish structure–activity relationships and elucidate the tandem electrocatalysis of individual Cu_2O and Co_3O_4 nanocubes alone but also their synergistic reaction, single-entity electrochemistry combined with identical location transmission electron microscopy was established.

We built on a previously suggested single-nanoparticle-on-a-nanoelectrode technique and first placed a single Cu_2O nanocube on the tip of a carbon nanoelectrode (CNE) was used to demonstrate the feasibility of the single-entity electrochemistry approach for the NO_3RR. CNEs with a flat disk surface were fabricated by focus ion beam (FIB) milling (Figure S14) according to an earlier reported strategy,[26]
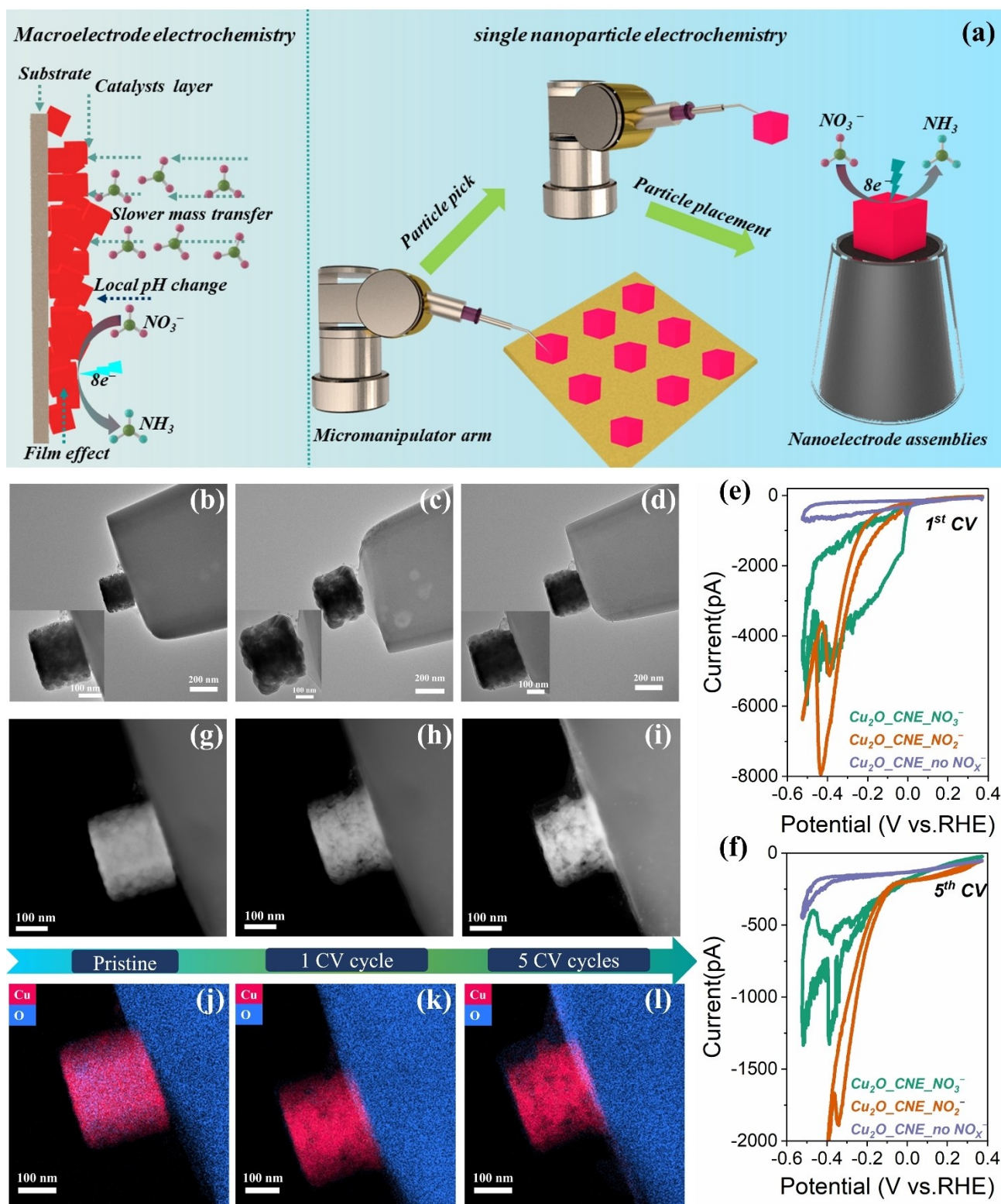
Figure 2. a) Schematic diagram of the macroelectrode electrochemistry and the process for fabrica-ting single nanoparticle electrochemistry. b)–d) TEM images of the three pristine single Cu_2O nanocubes on nanoelectrodes. (e and f) 1st CV and 5th CV of single Cu_2O nanocubes in 0.1 mol L^{-1} NaOH containing either 0.1 mol L^{-1} NO_3^- or 0.1 mol L^{-1} NO_2^- and pure 0.1 mol L^{-1} NaOH with a scan rate of 50 mV s^{-1}. g)–i) STEM images of a Cu_2O nanocube before (g), after the 1st CV cycle (h), and after the 5th CV cycles (i) in 0.1 mol L^{-1} NaOH containing 0.1 mol L^{-1} NO_3^- at a scan rate of 50 mV s^{-1}. j)–l) EDX elemental mapping of a Cu_2O nanocube before (j), after the 1st CV cycle (k), and after the 5th CV cycles (l) in 0.1 mol L^{-1} NaOH containing 0.1 mol L^{-1} NO_3^- at a scan rate of 50 mV s^{-1}.

followed by surface functionalization by diamine grafting to enhance the connection between CNE surface and the single particle. As illustrated in Figure 2a and Figure S15, a single well-defined Cu_2O nanocube was then selected, picked up, and precisely placed onto the tip of a CNE with a robotic micromanipulator system inside the SEM chamber. TEM images (Figure 2b–d) and EDX mapping (Figure S16) show three single Cu_2O nanocubes on CNE assemblies (Cu_2O_CNE) with the nanocubes firmly attached to the CNEs.

The NO_3RR activity of single Cu_2O_CNE assemblies was investigated by CV under the same conditions as used for the macroelectrode experiments. Notably, all CVs for single particles on CNEs are limited to 5 cycles due to the much faster reaction and speed of structure evolution compared to that on macroelectrodes.[15–17] Figures 2e and f show the significantly increased current and lower overpotentials in electrolyte containing NO_3^- or NO_2^-, indicating that the electrocatalytic activity is due to NO_x^- reduction. Moreover, a deactivation process was observed in both NO_3^- and NO_2^- containing electrolytes with an increasing number of CV cycles (Figure S17),[27] indicating a change in the surface activity of Cu-based NO_xRR electrocatalysts.

The Cu_2O_CNE nano-assemblies were investigated using identical location TEM to visualize the structural evolution of a single nanocube after different numbers of CV cycles in the electrolyte containing NO_3^-. The cubic structure was preserved (Figures 2g and h) after the 1st CV, but Cu started to leach out from the edge of the cube after the 1st CV cycle, as confirmed by the diminished Cu distribution in the EDX mapping (Figures 2j and k). EDX line scans before and after the 1st CV show a decreased content of O, suggesting the reduction of Cu_2O to metallic Cu (Figure S18). After the 5th CV cycle, Cu leaching becomes more pronounced, but the basic cubic structure is still maintained (Figures 2i and l). Cu_2O nanocubes show a similar structure evolution if investigated in an electrolyte containing NO_2^- or in the absence of any NO_x^- species (Figures S19 and S20).

This is supposedly due to the concomitant hydrogen evolution reaction at more negative potentials.[27] This hypothesis is supported by the improved structure stability before and after 5 CV cycles when the potential scan is limited to more positive potentials of less than -0.4 V (Figures S21 and S22). To provide direct visual evidence for the dynamic transformation of $Cu_2O + Co_3O_4$ during tandem catalysis, a $Cu_2O + Co_3O_4$ single particle arrangement with precise nano-placement of a single Cu_2O and a single Co_3O_4 nanocube was intended. Figure 3a illustrates how we fabricate a single-entity assembly with a single Cu_2O and a single Co_3O_4 cube placed together on one CNE to form a defined $Cu_2O + Co_3O_4$ tandem catalyst. Firstly, a single Cu_2O nanocube was placed on a specific location of the CNE using the micromanipulator arm inside the SEM. Subsequently, the micromanipulator arm picked up the Co_3O_4 nanocube and placed it next to the Cu_2O nanocube on the same CNE (Figures S23 and S24). Before placing the Co_3O_4 nanocube, the moving speed of the micromanipulator was adjusted to fine mode, and the previously placed Cu_2O was used as reference for placing the Co_3O_4 nanocube

accurately at the envisaged position on the CNE surface. Both cubes were carefully selected under SEM control before their placement on the CNE. The two particles nano-assemblies were then characterized by TEM, STEM, and corresponding EDX elemental line scans (Figure 3b–d). Three different relative placements of the two nanocubes were obtained, namely a CNE modified with two cubes next to each other ($Cu_2O + Co_3O_4$_CNE-1), two partially overlapping cubes ($Cu_2O + Co_3O_4$_CNE-2) and two spatially separated cubes ($Cu_2O + Co_3O_4$_CNE-3).

The electrochemical activity of the $Cu_2O + Co_3O_4$ nanoelectrode assemblies was investigated in the presence of NO_3^- and a single Co_3O_4 particle alone was also compared as control (Figure S25). The $Cu_2O + Co_3O_4$_CNE nano-assemblies exhibited substantially different catalytic activities compared to a single Cu_2O nanocube. The ratio of the change of reduction current at 0.35 V was compared to the 1st CV (Figure 3e), as a descriptor of the NO_3RR activity change trend of different single-particle nano-assemblies with increasing CV cycles.

In stark contrast to the single Cu_2O or Co_3O_4 cubes alone, $Cu_2O + Co_3O_4$_CNE-1 and $Cu_2O + Co_3O_4$_CNE-2 show a substantially increased NO_3RR current with the number of the CV cycles, indicating a continuously growing activity of $Cu_2O + Co_3O_4$ for the NO_3RR. This result can be well explained by assuming tandem catalysis in the case of $Cu_2O + Co_3O_4$, in which the NO_3RR on $Cu_2O + Co_3O_4$ can be divided into two sequential steps of the reduction of NO_3^- to NO_2^- on Cu_2O followed by the conversion of NO_2^- to NH_3 at the close-by located Co_3O_4 particle.

EDX mapping (Figures 3f and g) shows that both particles still existed on the CNE with a relatively independent form after 5 CV cycles, which excludes the possibility of alloying between the two particles during the reaction. $Cu_2O + Co_3O_4$_CNE-3 (two particles placed with a gap of around 100 nm) exhibits a similar activation process in the first 3 cycles in Figure 3e, suggesting that the tandem catalysis also works with two separated particles suggesting that the primarily produced NO_2^- can transfer to the nearby Co_3O_4 to finish the subsequent conversion of NO_2^- to NH_3, and simultaneously excludes any possibility of interfacial effects for improving NO_3RR activity. Then the reduction current decreased in the last two CVs, which is similar to the changes for the single particles alone. This result, together with the finding that all Cu was dissolved after 5 CV cycles (Figure 3h) further support the proposed tandem catalysis mechanism.

Cu_2O in $Cu_2O + Co_3O_4$ nanoelectrode assemblies shows a drastic morphology change compared to a single Cu_2O nanoelectrode assembly (Figures S26 and S27). At the same experimental conditions, the cubic structure of Cu_2O completely collapsed due to the massive leaching of Cu after 5 CV cycles in $Cu_2O + Co_3O_4$ nanoelectrode assemblies. This result can be well explained based on our previous study about tandem catalysis system, which high oxidative and corrosive nitrogen dioxide (NO_2) is produced at the Cu-based phase during NO_3RR tandem catalysis (NO_3^- to NO_2^-),[12] which greatly accelerates Cu leaching. On the other side, Co_3O_4 in $Cu_2O + Co_3O_4$ nanoelectrode assemblies maintained the cubic structure after 5 CV cycles similar to
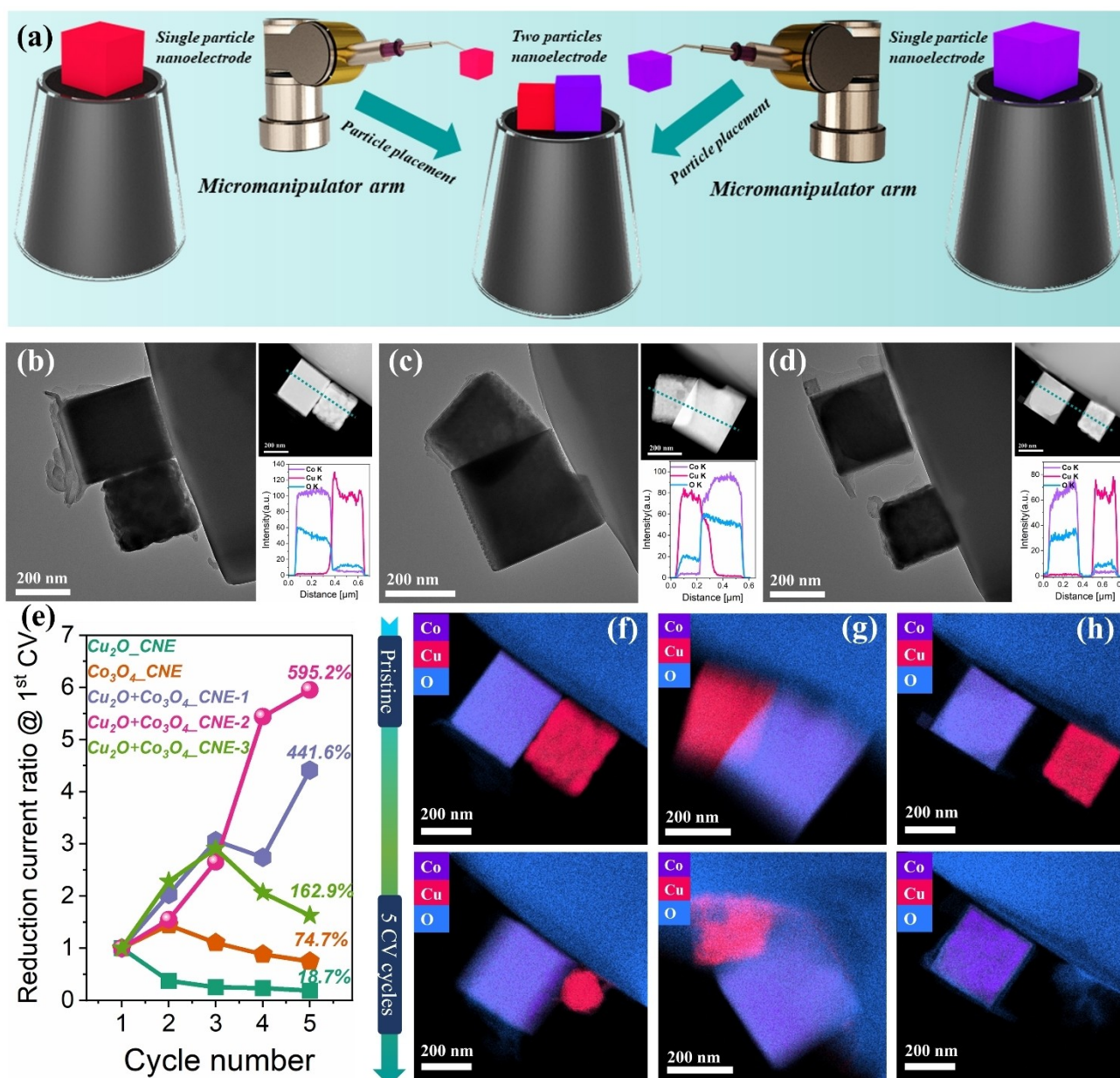
Figure 3. a) Schematic diagram of the fabrication process of two particles nanoelectrode assemblies. b)–d) TEM, STEM images, and corresponding EDX line scans of $Cu_2O+Co_3O_4$_CNE-1 (b), $Cu_2O+Co_3O_4$_CNE-2 (c), $Cu_2O+Co_3O_4$_CNE-3 (d). e) Plots showing the change in the ratio of the reduction current of Cu_2O, Co_3O_4, $Cu_2O+Co_3O_4$ nanoelectrode assemblies at −0.35 V (vs. RHE) compared to the 1st CV. f)–h) EDX mapping of $Cu_2O+Co_3O_4$_CNE-1 (f), $Cu_2O+Co_3O_4$_CNE-2 (g), $Cu_2O+Co_3O_4$_CNE-3 (h) before (top) and after 5 CV cycles (bottom).

the single Co_3O_4 nanoelectrode assembly (Figure S28). This can be ascribed to the fact that Co_3O_4 mainly converts NO_2^- to NH_3 during tandem catalysis avoiding the formation of NO_2. The structure evolution of $Cu_2O+Co_3O_4$ on the carbon nanoelectrode during NO_3RR corresponds well to results from macroelectrodes. The cubic structure of Cu_2O was completely disintegrated after ten hours of chronoamperometric electrolysis, while the cubic structure of Co_3O_4 was well preserved (Figure S29). Post-electrocatalysis EDX line scans show that the Cu_2O in $Cu_2O+Co_3O_4$_CNE-1 and $Cu_2O+Co_3O_4$_CNE-2 kept the high O content due to the high oxidative NO_2 (Figures S30 and 31), which is in stark

contrast to single Cu_2O (Figure S18). Co_3O_4 in $Cu_2O+Co_3O_4$ nanoelectrode assemblies shows a decreased O content, indicating the conversion of Co_3O_4 to lower oxidation states during the reaction (Figures S32 and S33).

To further confirm that the structural evolution in $Cu_2O+Co_3O_4$ is caused by tandem catalysis, a single Cu_2O particle was placed on the top of a single Co_3O_4 particle with only the Co_3O_4 particle in contact to the CNE surface denoted as $Cu_2O+Co_3O_4$_CNE-4 (Figure S34), in which electron transfer from the CNE to Cu_2O is limited by the relatively poor conductivity of Co_3O_4.[28] We expect that in this configuration tandem catalysis is largely suppressed and

the Cu_2O particle should not experience a drastic morphology change. The preservation of the cubic structure of Cu_2O after 5 CV cycles is shown in Figure S35.

In situ Raman spectroelectrochemistry under variation of the applied potentials in the presence of $0.1\ mol\,L^{-1}\ NO_3^-$ provides real-time insight into the phase evolution of the catalysts. All in situ Raman measurements were conducted in $0.01\ mol\,L^{-1}\ NaOH$ for protecting the water immersion objective, and $0.045\ mol\,L^{-1}\ Na_2SO_4$ was added to keep the ionic strength and the concentration of Na^+ identical to a $0.1\ mol\,L^{-1}\ NaOH$ solution. The Raman spectra of Cu_2O (Figure 4a) during the NO_3RR shows two bands at 982 and $1050\ cm^{-1}$, which are ascribed to the characteristic vibration modes of SO_4^{2-} and NO_3^-.[22,29] Notably, the peaks at 716 and $817\ cm^{-1}$ are from the carbon paper (Figure S36). The initially sharp Raman bands of Cu_2O at 218, 415, 523 as well as $628\ cm^{-1}$ start to weaken with increasing negative potentials, suggesting the reduction of Cu_2O to metallic Cu, which is consistent with the phase conversion observed in the single Cu_2O CNE assembly (Figure S18). The characteristic Co_3O_4 Raman peaks evolution at different applied potentials are shown in Figure 4b. The bands at 690 and $522\ cm^{-1}$, assigned to the A_{1g}, F_{2g} vibrational modes of Co_3O_4 are weak at potentials above $-0.1\ V$, and the F_{2g} peak disappeared at $-0.2\ V$.[21] Simultaneously, a Raman peak of $Co(OH)_2$ at $615\ cm^{-1}$ emerged and increased in intensity with increasing negative potentials,[30] which indicates the conversion of the Co_3O_4 phase to a lower oxidation state of $Co(OH)_2$ during the reaction. Raman peaks of $Co_3O_4+Cu_2O$ (Figure 4c) show similar phase evolution characteristics of both Co_3O_4 and Cu_2O alone. Two Raman peaks of CuO emerged at $-0.1\ V$ at 295 and $347\ cm^{-1}$ due to oxidation of Cu^0 by the initially formed intermediate nitrogen dioxide (NO_2), assuming that this is the only oxidative species produced during NO_3RR in Ar-saturated electrolyte.[12,31] This also explains the high O content after 5 CV cycles in $Cu_2O+Co_3O_4$ nanoelectrode assemblies (Figures S31 and S32).

Conclusion

We evaluated physically mixed $Cu_2O+Co_3O_4$ nanocubes as a tandem electrocatalyst for converting NO_3^- to NH_3 on a carbon paper macroelectrode and demonstrated significantly improved performance of $Co_3O_4+Cu_2O$ for NO_3^- to NH_3 reduction with Cu_2O or Co_3O_4 alone. An 85.4 % FE_{NH_3} and a high Y_{NH_3} of $12.76\ mg\,h^{-1}cm^{-2}$ was attained at an applied potential of $-0.3\ V$ vs RHE. To gain in-depth understanding of the synergistic action of both types of nanocube catalysts and to decipher mechanistic details of the tandem catalysis between Cu_2O and Co_3O_4, we established a single entity $Cu_2O+Co_3O_4$ nanocubes on a CNE tip approach with a precisely controlled placement of the two particles relative to each other. Single entity $Cu_2O+Co_3O_4$ nano-electrochemistry combined with identical location TEM revealed tandem catalysis by investigating the intrinsic activity changes and unveiled the structural evolution before and after the reaction. The phase evolution process observed from the single entity of $Cu_2O+Co_3O_4$ was further evidenced by in situ Raman spectroelectrochemistry.

Acknowledgements

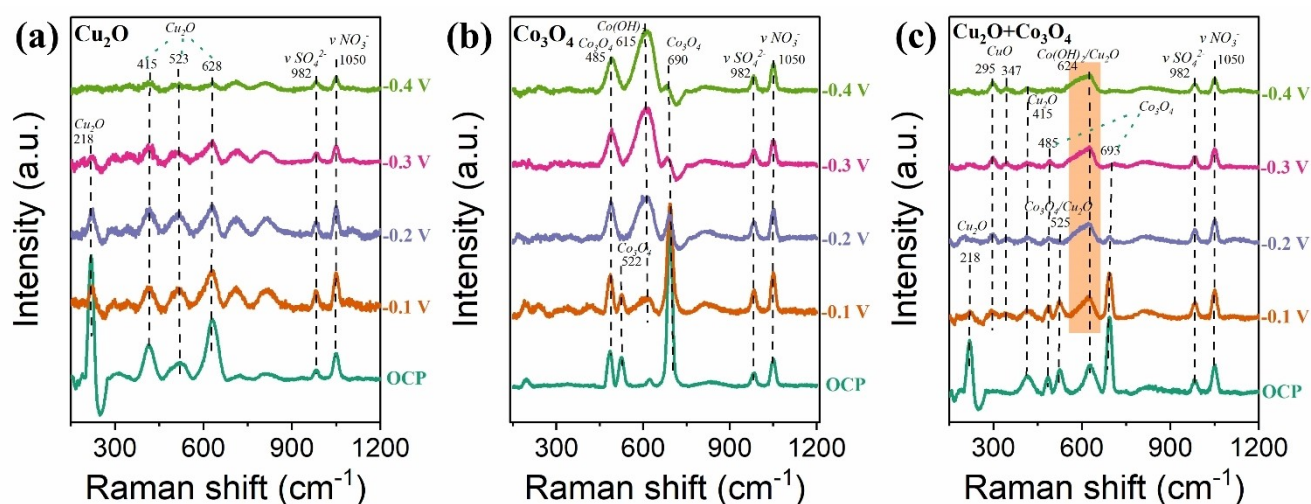**Figure 4.** a)–c) In situ Raman spectroelectrochemistry of Cu_2O (a), Co_3O_4 (b), $Cu_2O+Co_3O_4$ (c) at different applied potentials in electrolytes containing $0.1\ mol\,L^{-1}\ NO_3^-$, $0.045\ mol\,L^{-1}\ Na_2SO_4$ and $0.01\ mol\,L^{-1}\ NaOH$.

Conflict of Interest

The authors declare no conflict of interest.

Data Availability Statement

The data that support the findings of this study are available from the corresponding author upon reasonable request.

[1] a) V. Rosca, M. Duca, M. T. de Groot, M. T. M. Koper, *Chem. Rev.* **2009**, *109*, 2209; b) C. H. Christensen, T. Johannessen, R. Z. Sørensen, J. K. Nørskov, *Catal. Today* **2006**, *111*, 140; c) X. Zhang, E. A. Davidson, D. L. Mauzerall, T. D. Searchinger, P. Dumas, Y. Shen, *Nature* **2015**, *528*, 51.

[2] a) S. Licht, B. Cui, B. Wang, F.-F. Li, J. Lau, S. Liu, *Science* **2020**, *369*, 780; b) V. Kyriakou, I. Garagounis, A. Vourros, E. Vasileiou, M. Stoukides, *Joule* **2020**, *4*, 142; c) H. Liu, *Chin. J. Catal.* **2014**, *35*, 1619.

[3] a) D. R. MacFarlane, P. V. Cherepanov, J. Choi, B. H. Suryanto, R. Y. Hodgetts, J. M. Bakker, F. M. Ferrero Vallana, A. N. Simonov, *Joule* **2020**, *4*, 1186; b) H. Jin, L. Li, X. Liu, C. Tang, W. Xu, S. Chen, L. Song, Y. Zheng, S.-Z. Qiao, *Adv. Mater.* **2019**, *31*, 1902709; c) L. Zhang, X. Ji, X. Ren, Y. Ma, X. Shi, Z. Tian, A. M. Asiri, L. Chen, B. Tang, X. Sun, *Adv. Mater.* **2018**, *30*, 1800191.

[4] a) G.-F. Chen, X. Cao, S. Wu, X. Zeng, L.-X. Ding, M. Zhu, H. Wang, *J. Am. Chem. Soc.* **2017**, *139*, 9771; b) B. H. R. Suryanto, H.-L. Du, D. Wang, J. Chen, A. N. Simonov, D. R. MacFarlane, *Nat. Catal.* **2019**, *2*, 290.

[5] X. Guo, J. Gu, S. Lin, S. Zhang, Z. Chen, S. Huang, *J. Am. Chem. Soc.* **2020**, *142*, 5709.

[6] A. Stirling, I. Pápai, J. Mink, D. R. Salahub, *J. Chem. Phys.* **1994**, *100*, 2910.

[7] a) P. H. van Langevelde, I. Katsounaros, M. T. Koper, *Joule* **2021**, *5*, 290; b) Y. Wang, C. Wang, M. Li, Y. Yu, B. Zhang, *Chem. Soc. Rev.* **2021**, *50*, 6720.

[8] a) W. Teng, N. Bai, Y. Liu, Y. Liu, J. Fan, W.-X. Zhang, *Environ. Sci. Technol.* **2018**, *52*, 230; b) Y. Fernández-Nava, E. Marañón, J. Soons, L. Castrillón, *Bioresour. Technol.* **2008**, *99*, 7976.

[9] G. A. Cerrón-Calle, T. P. Senftle, S. Garcia-Segura, *Curr. Opin. Electrochem.* **2022**, *35*, 101062.

[10] a) Y. Yamada, C.-K. Tsung, W. Huang, Z. Huo, S. E. Habas, T. Soejima, C. E. Aliaga, G. A. Somorjai, P. Yang, *Nat. Chem.* **2011**, *3*, 372; b) S. Overa, T. G. Feric, A.-H. A. Park, F. Jiao, *Joule* **2021**, *5*, 8; c) P. B. O'Mara, P. Wilde, T. M. Benedetti, C. Andronescu, S. Cheong, J. J. Gooding, R. D. Tilley, W. Schuhmann, *J. Am. Chem. Soc.* **2019**, *141*, 14093; d) J. R. C. Junqueira, P. B. O'Mara, P. Wilde, S. Dieckhöfer, T. M. Benedetti, C. Andronescu, R. D. Tilley, J. J. Gooding, W. Schuhmann, *ChemElectroChem* **2021**, *8*, 4848; e) G.-F. Chen, Y. Yuan, H. Jiang, S.-Y. Ren, L.-X. Ding, L. Ma, T. Wu, J. Lu, H. Wang, *Nat. Energy* **2020**, *5*, 605.

[11] a) H. Niu, Z. Zhang, X. Wang, X. Wan, C. Shao, Y. Guo, *Adv. Funct. Mater.* **2021**, *31*, 2008533; b) M. Duca, J. R. Weeks, J. G. Fedor, J. H. Weiner, K. A. Vincent, *ChemElectroChem* **2015**, *2*, 1086.

[12] W. He, J. Zhang, S. Dieckhöfer, S. Varhade, A. C. Brix, A. Lielpetere, S. Seisel, J. R. C. Junqueira, W. Schuhmann, *Nat. Commun.* **2022**, *13*, 1129.

[13] a) Y. Wang, P. Han, X. Lv, L. Zhang, G. Zheng, *Joule* **2018**, *2*, 2551; b) E. L. Clark, C. Hahn, T. F. Jaramillo, A. T. Bell, *J. Am. Chem. Soc.* **2017**, *139*, 15848; c) T. T. H. Hoang, S. Verma, S. Ma, T. T. Fister, J. Timoshenko, A. I. Frenkel, P. J. A. Kenis, A. A. Gewirth, *J. Am. Chem. Soc.* **2018**, *140*, 5791.

[14] L. A. Baker, *J. Am. Chem. Soc.* **2018**, *140*, 15549.

[15] J. Zhang, T. Quast, W. He, S. Dieckhöfer, J. R. C. Junqueira, D. Öhl, P. Wilde, D. Jambrec, Y.-T. Chen, W. Schuhmann, *Adv. Mater.* **2022**, *34*, 2109108.

[16] T. Quast, S. Varhade, S. Saddeler, Y.-T. Chen, C. Andronescu, S. Schulz, W. Schuhmann, *Angew. Chem. Int. Ed.* **2021**, *60*, 23444; *Angew. Chem.* **2021**, *133*, 23634.

[17] T. Quast, H. B. Aiyappa, S. Saddeler, P. Wilde, Y.-T. Chen, S. Schulz, W. Schuhmann, *Angew. Chem. Int. Ed.* **2021**, *60*, 3576; *Angew. Chem.* **2021**, *133*, 3619.

[18] H. B. Aiyappa, P. Wilde, T. Quast, J. Masa, C. Andronescu, Y.-T. Chen, M. Muhler, R. A. Fischer, W. Schuhmann, *Angew. Chem. Int. Ed.* **2019**, *58*, 8927; *Angew. Chem.* **2019**, *131*, 9021.

[19] M. Arenz, A. Zana, *Nano Energy* **2016**, *29*, 299.

[20] Y. Deng, A. D. Handoko, Y. Du, S. Xi, B. S. Yeo, *ACS Catal.* **2016**, *6*, 2473.

[21] V. G. Hadjiev, M. N. Iliev, I. V. Vergilov, *J. Phys. C* **1988**, *21*, 199.

[22] Y. Zhao, X. Chang, A. S. Malkani, X. Yang, L. Thompson, F. Jiao, B. Xu, *J. Am. Chem. Soc.* **2020**, *142*, 9735.

[23] F.-Y. Chen, Z.-Y. Wu, S. Gupta, D. J. Rivera, S. V. Lambeets, S. Pecaut, J. Y. T. Kim, P. Zhu, Y. Z. Finfrock, D. M. Meira, G. King, G. Gao, W. Xu, D. A. Cullen, H. Zhou, Y. Han, D. E. Perea, C. L. Muhich, H. Wang, *Nat. Nanotechnol.* **2022**, *17*, 759–767.

[24] R. Y. Hodgetts, A. S. Kiryutin, P. Nichols, H.-L. Du, J. M. Bakker, D. R. MacFarlane, A. N. Simonov, *ACS Energy Lett.* **2020**, *5*, 736.

[25] a) P. Wilde, S. Barwe, C. Andronescu, W. Schuhmann, E. Ventosa, *Nano Res.* **2018**, *11*, 6034; b) J. Ryu, A. Wuttig, Y. Surendranath, *Angew. Chem. Int. Ed.* **2018**, *57*, 9300; *Angew. Chem.* **2018**, *130*, 9444.

[26] P. Wilde, T. Quast, H. B. Aiyappa, Y.-T. Chen, A. Botz, T. Tarnev, M. Marquitan, S. Feldhege, A. Lindner, C. Andronescu, et al., *ChemElectroChem* **2018**, *5*, 3083.

[27] E. Pérez-Gallent, M. C. Figueiredo, I. Katsounaros, M. T. Koper, *Electrochim. Acta* **2017**, *227*, 77.

[28] S. A. Makhlouf, Z. H. Bakr, K. I. Aly, M. S. Moustafa, *Superlattices Microstruct.* **2013**, *64*, 107.

[29] a) M. Xu, J. P. Larentzos, M. Roshdy, L. J. Criscenti, H. C. Allen, *Phys. Chem. Chem. Phys.* **2008**, *10*, 4676; b) N. Bodappa, M. Su, Y. Zhao, J.-B. Le, W.-M. Yang, P. Radjenovic, J.-C. Dong, J. Cheng, Z.-Q. Tian, J.-F. Li, *J. Am. Chem. Soc.* **2019**, *141*, 12192.

[30] a) J. Yang, H. Liu, W. N. Martens, R. L. Frost, *J. Phys. Chem. C* **2010**, *114*, 111; b) Y.-C. Liu, J. A. Koza, J. A. Switzer, *Electrochim. Acta* **2014**, *140*, 359.

[31] a) A. P. Litvinchuk, A. Möller, L. Debbichi, P. Krüger, M. N. Iliev, M. M. Gospodinov, *J. Phys. Condens. Matter* **2013**, *25*, 105402; b) L. Debbichi, M. C. Marco de Lucas, J. F. Pierson, P. Krüger, *J. Phys. Chem. C* **2012**, *116*, 10232.
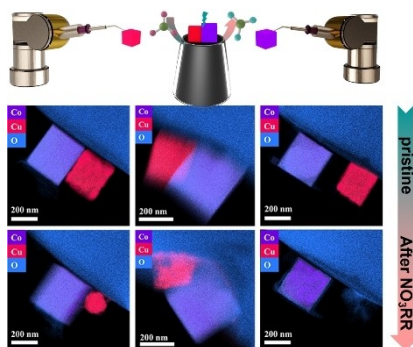
Research Articles

Nitrate Reduction

J. Zhang, W. He, T. Quast, J. R. C. Junqueira, S. Saddeler, S. Schulz, W. Schuhmann* ———— **e202214830**

Single-entity Electrochemistry Unveils Dynamic Transformation during Tandem Catalysis of Cu$_2$O and Co$_3$O$_4$ for Converting NO$_3^-$ to NH$_3$

A rational catalyst design strategy is vital for a highly efficient conversion of NO$_3^-$ to NH$_3$. Cu$_2$O + Co$_3$O$_4$ tandem catalyst exhibit a much higher NH$_3$ yield rate than the single component alone. More importantly, we confirmed tandem catalysis by placing individual single Cu$_2$O and Co$_3$O$_4$ on carbon nanoelectrode. Using single-entity electrochemistry and identical-location TEM we unveiled the dynamic transformation caused by tandem catalysis.